One-Pot Synthesis of Bioinspired Peptide-Decorated Apatite Nanoparticles for Nanomedicine

Mathilde Guérin, Aurélien Lebrun, Liisa Kuhn, Thierry Azaïs, Guillaume Laurent, Olivier Marsan, Christophe Drouet, Gilles Subra

RESEARCH ARTICLE

NANO · MICRO small
www.small-journal.com

One-Pot Synthesis of Bioinspired Peptide-Decorated Apatite Nanoparticles for Nanomedicine

Mathilde Guérin, Aurélien Lebrun, Liisa Kuhn, Thierry Azaïs, Guillaume Laurent, Olivier Marsan, Christophe Drouet, and Gilles Subra**

Hybrid organic–inorganic bio-inspired apatite nanoparticles (NPs) are attractive for biomedical applications and especially in nanomedicine. Unfortunately, their applications in nanomedicine are limited by their broad particle size distributions and uncontrolled drug loading due to their multistep synthesis process. Besides, very few attempts at exposing bioactive peptides on apatite NPs are made. In this work, an original one-pot synthesis of well-defined bioactive hybrid NPs composed of a mineral core of bioinspired apatite surrounded by an organic corona of bioactive peptides is reported. Dual stabilizing-bioactive agents, phosphonated polyethylene glycol-peptide conjugates, are prepared and directly used during apatite precipitation i) to form the organic corona during apatite precipitation, driving the size and shape of resulting hybrid NPs with colloidal stabilization and ii) to expose peptide moieties (RGD or YIGSR sequences) at the NPs periphery in view of conferring additional surface properties to enhance their interaction with cells. Here, the success of this approach is demonstrated, the functionalized NPs are fully characterized by Fourier-transform infrared, Raman, X-ray diffraction, solid and liquid state NMR, transmission electron microscopy, and dynamic light scattering, and their interaction with fibroblast cells is followed, unveiling a synergistic proliferative effect.

1. Introduction

Calcium phosphate apatites represent a large family of mineral compounds[1] relevant to many domains, due to their natural presence in bones and teeth but also in phosphate-bearing minerals of geological relevance. These compounds derive from stoichiometric hydroxyapatite HA, $Ca_{10}(PO_4)_6(OH)_2$. While the composition of dental enamel is close to that of HA, apatites found in dentin and bone are moderately crystallized due to their nonstoichiometry and nanocrystalline character, and their chemical formula can often be approximated to $Ca_{10-x}(PO_4)_{6-x}(HPO_4)_x(OH)_{2-x}$ ($0 \leq x \leq 2$).[2]

Synthetic "biomimetic" apatite powders can be prepared by co-precipitation or hydrothermal methods,[3] and have been studied for various applications as bone substitutes or implant coating.[4–6] Moreover, such nonstoichiometric nanocrystalline apatites exhibit an exceptional surface reactivity allowing for adsorption of a large variety of (bio)molecules/drugs, thus widening their range of applications in (nano)medicine. Combination of drugs/(bio)molecules to apatite particles can provide several advantages over free molecules, e.g., for improving the solubility of hydrophobic therapeutic agents, reducing their toxicity, avoiding the early metabolization of active agents, and/or improving their distribution to a specific target. In previous studies, several molecular species such as enzymes,[7] growth factors,[8] drugs,[9–15] antibodies[16,17] have been associated with apatite compounds with the view to infer additional functionalities in link with clinical needs. However, these approaches have systematically been developed via multistep processes, requiring

M. Guérin, A. Lebrun, G. Subra
IBMM
CNRS
Université de Montpellier
1919 Route de Mende, Montpellier 34090, France
E-mail: gilles.subra@umontpellier.fr

M. Guérin, O. Marsan, C. Drouet
CIRIMAT
CNRS
Université de Toulouse
Ensiacet, 4 allee Emile Monso, Toulouse cedex 4 31030, France
E-mail: christophe.drouet@toulouse-inp.fr

L. Kuhn
Biomedical Engineering
UConn School of Dental Medicine
263 Farmington Avenue, MC1721, Farmington, CT 06030-1721, USA

T. Azaïs, G. Laurent
Laboratoire de Chimie de la Matière Condensée de Paris
Sorbonne Université and CNRS
4 place Jussieu, Paris 75005, France

The ORCID identification number(s) for the author(s) of this article can be found under https://doi.org/10.1002/smll.202306358

DOI: 10.1002/smll.202306358

preliminary apatite synthesis and subsequent adsorption step(s).

One difficulty comes from the natural tendency for apatite crystals to agglomerate, thus leading to uncontrolled particle sizes/shapes limiting nanomedical applications. Previous works showed that adding a stabilizing agent during apatite precipitation could limit the agglomeration process. Such molecules exposed typically an anionic end group (e.g., phosphate or phosphonate) capable of interacting with Ca^{2+} ions from the surface of apatite nanocrystals.[18,19] AEP (2-amino ethyl phosph(on)ate) was used, e.g., as stabilizing agent, exploiting the positive charge of the amino group to provide electrostatic repulsion.[18] Also, phosphonated polyethylene glycol (P(PEG)) can prevent particle agglomeration, by steric hindrance.[20] In this view, the length of the PEGylated chain allowed obtaining submicron to nanoscale colloidal particles relevant to dermatology,[20] hematology,[21] or oncology.[10,22,23] However, these stabilizing agents being not bioactive by themselves, it was necessary to co-adsorb other molecular moieties thus leading to competitive adsorption phenomena. Also, no control of the grafting density was reported on apatite nanoparticles (NPs), to the best of our knowledge.

In this context, being able to obtain colloidal apatite NPs while adjoining biological properties via the stabilizing agent itself appears as an extremely appealing innovative strategy. In this regard, peptides are another family of bioinspired compounds, which may exhibit a wealth of bioactive properties and could be envisaged for this goal. Yet, to this day, peptide-decorated apatite particles have not been reported, except for one recent study for the treatment of cystic fibrosis.[24] In this study, the authors functionalized apatite NPs with a cyclic antibacterial peptide, Colistin, with a two-step process; i) stabilization of apatite NPs by using citrate ions as stabilizing agents allowing a negative charge screen around the NPs and ii) the adsorption of Colistin thanks to an electrostatic interaction between its primary amine and the apatite surface. This two-step process led to increasing of particles size (95 to 213 nm) and a destabilization of the colloidal suspension.[9]

2. Results and Discussion

Therefore, the present work aimed at establishing a synthetic pathway to a family of well-defined hybrid apatite-peptide NPs via a versatile one-pot synthesis approach that could be of interest for health applications ranging from nanomedicine to tissue engineering. To this aim, we first designed and synthesized phosphonate-containing peptide PEG conjugates that could play a dual role of stabilizing agent and bioactive moiety.

We chose to use P(PEG) rather than AEP as apatite bonding moiety due to better stabilizing properties reported.[20] The addition of the peptide on the free amine of AEP would disrupt the electrostatic repulsion and thus the stabilization of the apatite NPs because ammonium ions would not be present on the apatite surface. The use of P(PEG) would not only allow the addition of the peptide without disrupting its stabilizing effect to obtai NPs of controlled size, but also would move the peptide away from the apatite surface thus limiting apatite/peptide interactions.

Noteworthy, PEGylation is extensively used to improve therapeutic peptides, biomolecules, and NPs biodisponibility.[25] In the latter case, when the NPs have to interact specifically on cell membrane receptors, ligands can be conjugated at the end of PEG chains in extended conformation all around the particle.[26]

We took inspiration from these studies hypothesizing that adding a peptide of less than 1 kDa at the end of an ≈68-mer PEG chain would have little or no impact on the stabilizing behavior of PEG whatever the amino acid sequence. To demonstrate the versatility of the method, we selected two biologically relevant peptide sequences, namely, Ac-LRGDNK-NH_2 (referred to as RGD in this work, pH = 8.2) and H-GDPGYIGSR-NH_2 (referred to as YIGSR, pH = 7.0), where the RGD and YIGSR moieties, respectively, derive from fibronectin[27] and laminin,[28–30] two important extracellular matrix proteins. These sequences have been described promoting cell adhesion and proliferation.[27,28,31,32]

The synthesis of the apatite/peptide hybrid NPs is summarized in **Figure 1**, including the preliminary preparation of the phosphonated PEG peptide conjugates. C-terminal amidated peptides Ac-LRGDNK-NH_2 **1** and H-GDPGYIGSR-NH_2 **2** were synthesized on Rink Amide ChemMatrix resin (0.47 mmol g^{-1}) by Fmoc/tBu strategy. The peptides were, respectively, obtained with 98% and 95% purity and used without purification. In parallel, the $PO_3Et_2CH_2CH_2CO$-(PEG3K)-COOH **8** was prepared by reacting selectively the free primary amine of NH_2-PEG3K-COOH **7** with activated 1-(2-diethoxyphosphorylethyl) benzotriazole **5** obtained in two steps from triethylphosphonopropianate **3**.[33] To avoid the troublesome separation of PEG-containing compounds **7** and **8**, compound **5** was used in excess to quantitatively obtain the desired compound **8**. The excess of **5** was removed with several ethylacetate washings after recovering it by a diethylether precipitation. Diethyl phosphonated PEG-peptide conjugates, $PO_3Et_2CH_2CH_2CO$-PEG3K-Peptide **9** and **10** and $PO_3Et_2CH_2CH_2CO$-PEG3K-NEt_2 **11** were prepared in solution. Indeed, the direct introduction of **8** on the peptide anchored on solid support proved to be inefficient due to steric hindrance of the polymer matrix. Conjugates **9**, **10**, and **11** were obtained by coupling the carboxylic acid of **8** activated by Hexafluorophosphate Azabenzotriazole Tetramethyl Uronium/N,N-Diisopropylethylamine (HATU/DIEA) with the free N-terminal group of **2**, the ϵ-amino group of lysine side chain of compound **1** or/and diethylamine, respectively. It may be noted that peptides and diethylamine were used in slight excess to facilitate workup of the reaction. The desired products and the excess of corresponding reactants were also recovered after a diethylether precipitation. The reactants were removed with several acetone washings. Finally, the deprotection of diethylphosphonate was achieved through McKenna et al.[34] reaction under inert condition with bromotrimethylsilane[35–38] overnight to quantitatively yield the desired products $PO_3H_2CH_2CH_2CO$-PEG3K-Peptide (named P(PEG3K)-Peptide) **12**, **13** and $PO_3H_2CH_2CH_2CO$-PEG3K-NEt_2 (named P(PEG3K)-NEt_2) **14**. This reaction was monitored at each stage by ^{31}P and ^{1}H liquid-state NMR.

The next stage of the synthesis consisted in the direct precipitation of the apatite phase in the presence of the new stabilizing conjugates **12**, **13**, and **14**. The precipitation conditions were inspired from previous works on AEP.[19,39] Briefly, the suspension was obtained by first mixing, in deionized water, a calcium nitrate solution (1.217 mmol, 1.625 mL) with a stabilizing agents solution containing phosphonated conjugates (0.020 mmol total concentration, 3.125 mL). The pH was adjusted to 9–10 with few

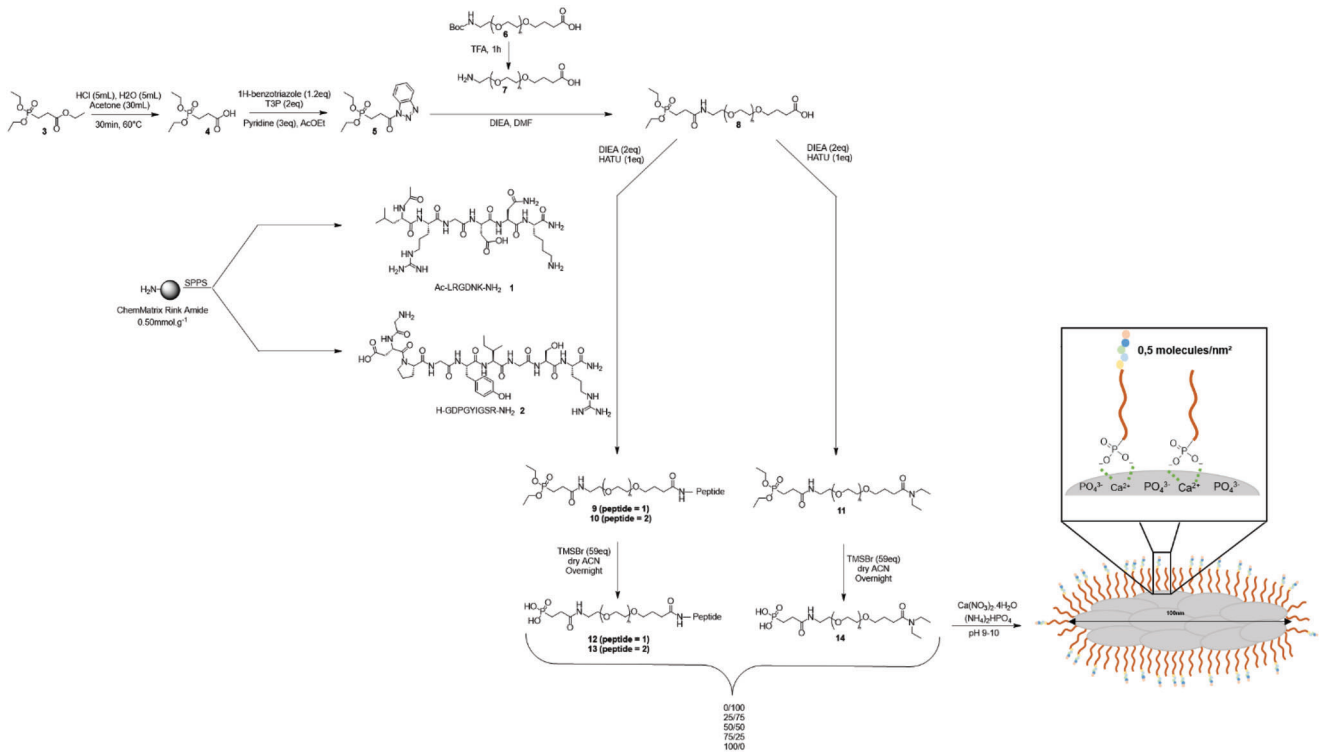

Figure 1. Synthesis of hybrid peptide apatite nanoparticles.

drops of ammonia to obtain the deprotonated form R-PO_3^{2-} of the organic phosphonate moiety, thus improving the interactions with calcium ions. Then, an ammonium hydrogen phosphate solution (0.405 mmol, 1.625 mL) was added to the mixture and pH was readjusted as previously to 9–10. At this step, a white calcium phosphate precipitate formed, which was matured at 100 °C for 16 h. In view of biological use, the NPs were purified by dialysis to remove the unreacted ions or organic molecules using a previously described methodology.[40] The preparation of a "reference" noncolloidal apatite sample, following exactly the same procedure as above but in the absence of any stabilizing agent, was already reported in previous works, along with its main physicochemical features (close-to-stoichiometry apatite).[18,39]

The first hybrid material was prepared with P(PEG3K)-NEt_2 compound **14** (i.e., without peptide sequence). Different amounts of **14** were tested to modulate the R-PO_3H_2/Ca molar ratio, from 0.001 to 0.128 (**Table 1**) to identify the optimal conditions for obtaining stable colloids, but also to examine the impact of this ratio on the shape, size, and chemical nature of the apatite phase of NPs. Whatever the P(PEG3K)-NEt_2/Ca starting proportions tested, colloidal suspensions were successfully obtained (NPs 1–6), thus confirming the stabilizing role of this P(PEG3K)-based methodology. The amount of organic linker X-ray diffraction (XRD) analyses clearly showed a crystallographic signature of an apatitic phase close to the bone mineral for each sample but a decrease of crystallinity could be observed as the R-PO_3H_2/Ca ratio increased until reaching a compound close to amorphous for the highest ratio at 0.128 (Figure S1 in the Supporting Information). The presence of a contribution on the XRD pattern at $2\theta = 23°$ can also be noted, which can be attributed to some degree of ordering of the long PEG chains in the dried state, in a similar way as previously reported.[20]

Moreover, dynamic light scattering (DLS) was carried out to evaluate the hydrodynamic diameter D_h of these NPs 1 to 6 which could be considered homogenous (polydispersity index (PdI) between 0.2 and 0.3) with a D_h value ranging from 391 nm for the ratio equal to 0.005 down to 126 nm for the highest ratio (Table 1). DLS is more suited to analyze spherical objects, thus transmission electron microscopy (TEM) analyses were performed to in depth examine the particles size and shape (**Figure 2**a). TEM imaging pointed out the polycrystalline character of the NPs, as is customary for apatitic compounds and confirmed the DLS results. Indeed, the particle size was observed to vary from 153 nm in length/35 nm in width for an R-PO_3H_2/Ca ratio of 0.001 down to 70 nm in length/59 nm in width for a ratio of 0.128 (Table 1). Considering that TEM is performed on dried samples while DLS gives the hydrodynamic diameter in solution, the value of 117 nm in length (e.g., NPs 4) agrees rather well with the 167 nm found by DLS (which is more informative on the largest dimension of anisotropic particles due to a greater impact on the laser obscuration).

The lower the amount of P(PEG3K)-NEt_2 stabilizing agent is involved in the synthesis, the lower the number of stabilizing agents is present around the NPs (confirmed by ERETIC ^{31}P liquid NMR—Table 1), thus inducing an increase in the size of the NPs because the steric hindrance was minimized.

These analyses confirmed that monomodal colloidal NPs could be obtained by this strategy, with a size that can be controlled through the amount of stabilizing agent introduced, which allow to match specific biological application

Table 1. Overview of the hybrid apatite NPs prepared in this work with their main physicochemical characteristics.

Starting molar ratios					DLS zeta potential			TEM		Quantitative ^{1}H NMR			ERETIC ^{31}P NMR			Grafting density Flory's equation		
Id	R-PO_3H_2/Ca	%14	%12	%13	Size [nm]	PdI	ζ at pH 7.2 [mV]	Mean width [nm]	Mean length [nm]	% 14	% 12	% 13	[R-PO_3H_2] [× 10^{-3} M]	[RGD] 1 [× 10^{-3} M]	[YIGSR] 2 [× 10^{-3} M]	σ (molecules nm^{-2})	Rf/D	Conformational regime
NPs 1	0.001	100	/	/	346 ± 1.26	0.27	7.2 ± 6.73	35	153	/	/	/	0.98	/	/	0.02	0.55	Intermediate
NPs 2	0.005	100	/	/	391 ± 7.61	0.28	4.8 ± 3.53	52	151	/	/	/	2.19	/	/	0.07	1.07	Brush
NPs 3	0.008	100	/	/	388 ± 0.92	0.23	4.0 ± 12.4	24	176	/	/	/	2.27	/	/	0.13	1.43	Brush
NPs 4	0.016	100	/	/	167 ± 4.88	0.24	1.7 ± 7.44	25	117	/	/	/	2.76	/	/	0.23	1.90	Brush
NPs 5	0.032	100	/	/	147 ± 2.23	0.25	1.9 ± 4.24	27	108	/	/	/	5.11	/	/	4.97	8.91	Brush
NPs 6	0.128	100	/	/	126 ± 6.66	0.32	1.6 ± 5.63	59	70	/	/	/	6.68	/	/	7.64	9.45	Brush
NPs 7	0.016	/	100	/	154 ± 0.83	0.25	−0.2 ± 0.10	50	133	0	100	/	2.25	2.25	/	1.05	4.09	Brush
NPs 8	0.016	25	75	/	113 ± 4.51	0.13	0.7 ± 0.11	32	84	60	40	/	2.27	0.67	/	0.43	4.44	Brush
NPs 9	0.016	50	50	/	109 ± 0.34	0.13	0 ± 0.23	31	101	80	20	/	2.95	0.44	/	0.47	4.57	Brush
NPs 10	0.016	75	25	/	102 ± 2.21	0.13	3.2 ± 0.33	40	82	92	8	/	3.49	0.21	/	0.59	4.92	Brush
NPs 11	0.016	/	/	100	204 ± 1.52	0.26	−0.46 ± 0.21	33	101	0	/	100	1.91	/	1.91	0.55	2.96	Brush
NPs 12	0.016	25	/	75	104 ± 1.85	0.13	−0.9 ± 0.25	31	84	33	/	66	2.91	/	1.79	0.47	4.42	Brush
NPs 13	0.016	50	/	50	112 ± 0.90	0.11	0.4 ± 0.15	36	91	67	/	33	3.48	/	1.06	0.48	4.59	Brush
NPs 14	0.016	75	/	25	107 ± 0.95	0.11	3.7 ± 0.40	27	103	80	/	20	3.86	/	0.71	0.62	5.24	Brush

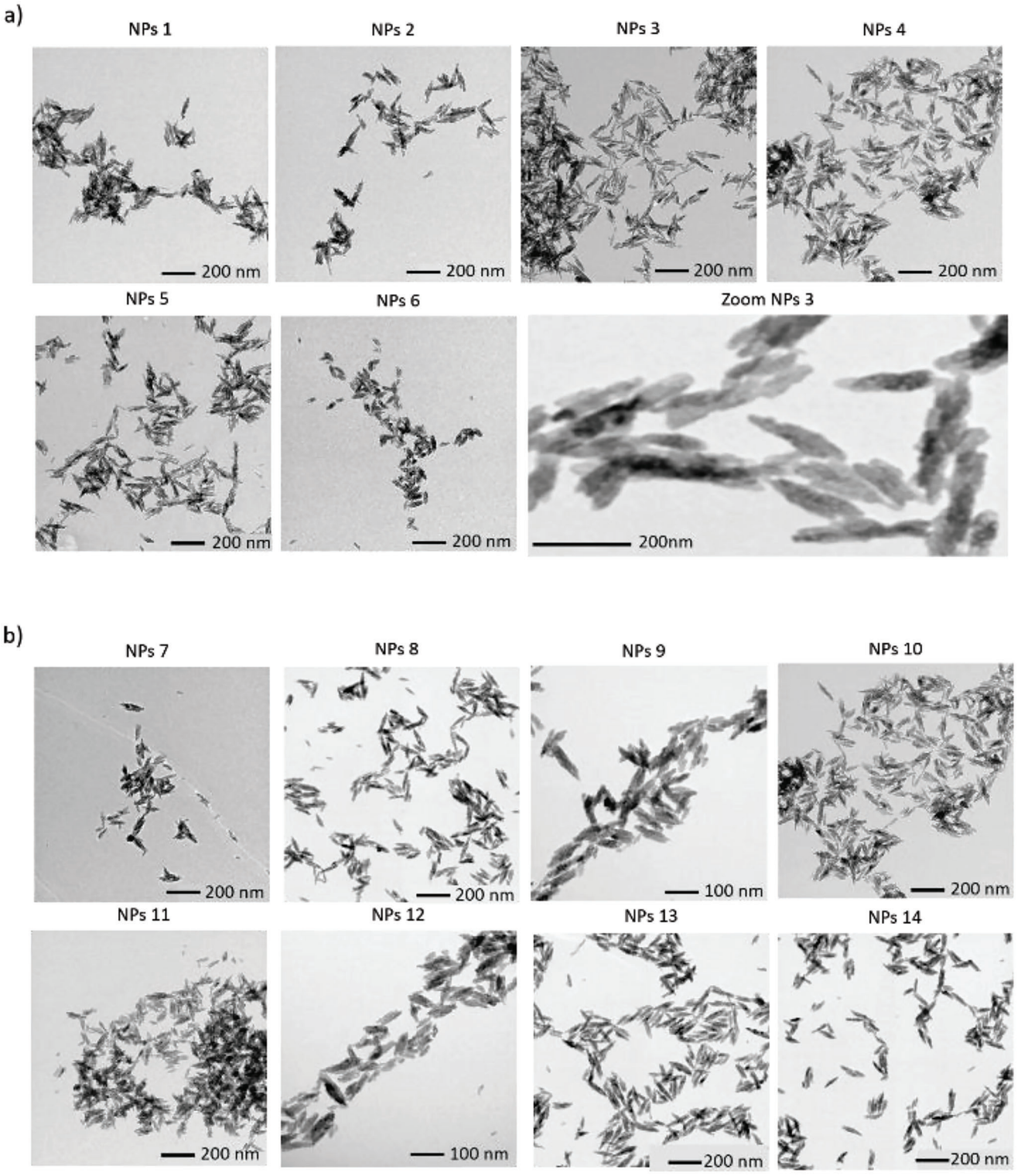

Figure 2. TEM images of a) NPs 1–6 stabilized with P(PEG3K)-NH_2 and P(PEG3K)-RGD; b) and P(PEG3K)-NH2; c) NPs 7-14 stabilized with P(PEF3K)-NH2 and P(PEG3K)-YIGSR.

requirements. Noteworthy, colloidal suspensions remained stable over 6 months (Table S1, Supporting Information), demonstrating the relevance of the P(PEG3K)-based stabilization.

Based on these results, the ratio R-PO_3H_2/Ca equal to 0.016 was chosen for the following experiments with the P(PEG3K)-Peptide because it seemed to be a good compromise to obtain nanosized particles, a biomimetic apatite close to the bone mineral, and a controlled grafting density sufficiently important in view of further analyses and biological experiments. Moreover, the brush regime obtained with this ratio could provide well-exposed peptidic moieties for facilitated interactions with cells/tissues/outer environments.

The second family of hybrid NPs (NPs 7–14, Table 1) was prepared as previously but with various molar ratios between new stabilizing agents P(PEG3K)-Peptide **12**, **13** and a simple stabilizing agent P(PEG3K)-NEt_2 **14** (100/0, 75/25, 50/50, 25/75, 0/100) to observe the influence of the P(PEG3K)-Peptide and to test the co-administration of two molecules. Whatever the nature of the peptides and the ratios tested, colloidal suspensions were successfully obtained confirming the hypothesis that the peptide moieties had no influence. The raw peptide loading yield in this work was found to be in the range 30–60% depending on the PEG/PEG-peptide ratio used (Table S3, Supporting Information). Note, however, that the usual loading yield concept cannot apply here since the degree of peptide fixation (through the phosphonated PEG linker) directly relates to the concentration of the organic conjugate in the apatite precipitating medium.

DLS analyses of these NPs 7–14 were found to exhibit a narrow monomodal distribution (PdI between 0.11 and 0.26) with a D_h value comprised between 102 and 204 nm (with a tendency to increase smoothly upon peptide functionalization) with an average of ≈125 nm (Table 1). For the same reasons as before, TEM analyses were performed and homogenous overall rod shape was evidenced, with a mean length of ≈97 nm and a mean width of ≈35 nm (Figure 2b).

Further compositional and structural investigations were carried out to characterize deeper such peptide-decorated NPs. A liquid-state NMR methodology was developed to determine the composition of the NPs. For that purpose, 1 mL of colloidal suspension was freeze dried and the NPs obtained were dissolved in acidic condition (pH ∼1) by adding 100 µL of HCl solution (1 M). Indeed, at acidic pH < 4–5, the apatite phase gets totally dissolved, thus releasing HPO_4^{2-} ions and the grafted P(PEG3K)-Peptide **12** or **13** and/or P(PEG3K)-NEt_2 **14**. ERETIC ^{31}P NMR analyses were then carried out to determine the organic phosphonate content in NPs 7–14. Indeed, the inorganic phosphate ions (0 ppm) and the organic phosphonate (25 ppm) can be separately integrated to calculate their concentration. Also, quantitative ^{1}H NMR was performed to distinguish the P(PEG3K)-Peptide **12** and **13** from P(PEG3K)-NEt_2 **14**, for the NPs 7–10 and 11–14 decorated, respectively, with the peptides RGD or YIGSR. By integrating the ^{1}H NMR signals from the –CH_3' of the diethylamine (1.23 ppm), the –CH_3 from the isopropyl of the Leucine (0.93–0.88 ppm), and the aromatic protons of the Tyrosine (6.84 ppm), we obtained the molar content of each organic moiety and therefore the amounts of molecules grafted on the NPs.

By combining these ^{1}H and ^{31}P liquid-state NMR data, we finally obtained the peptide content in 1 mL of colloidal suspensions (Table 1). This information is of importance for further biological assays. As expected, as the proportion of P(PEG3K)-NEt_2 **30** increased, the size of the particles decreased whatever the peptide studied from about 200 nm for the highest ratio (NPs 7 and 11) to 100 nm for the lowest ratio (NPs 10 and 14) (Table 1). These findings suggest that the steric hindrance caused by P(PEG3K)-Peptide is more important than for P(PEG3K)-NEt_2 alone, hence the somewhat reduced amount of P(PEG3K)-Peptide actually grafted on the NPs surface. Moreover, the presence of the peptides at the end of the PEG chain did not prevent the formation of a colloidal suspension with a monomodal dispersion of NPs, because the PdI was comprised between 0.11 and 0.26. This could be explained because the maximum length of an amino acid residue is estimated to be 3.01 Å. The RGD and YIGSR peptides possessing, respectively, six and nine amino acids have thus an estimated length of ≈18 and ≈27 Å, respectively. These values represent about 10% of the length of the PEG chain (≈206 Å). This proportion is small enough not to disturb the colloidal stability of the NPs, but it still represents a slight volume increase at the external end of the P(PEG3K)-Peptide conjugates that could explain our above-mentioned observations.

To confirm these hypotheses, the grafting density σ around the NPs was calculated from the previous liquid-state NMR data. Considering that the NPs have a rod-like morphology as indicated by TEM (Figure 2b), and assuming a cylindrical shape, the volume of an average NPs as well as its corresponding surface could be estimated (≈10^8 nm^2). Whatever the NP, the grafting density (P(PEG3K)-NEt_2 + P(PEG3K)-Peptide) was the same with a value of $\sigma = 0.5$ molecules nm^{-2} (Table 1). It may be noted that this density can be modulated by modifying the amount of organic moieties containing the P(PEG3K) end group, as depicted in Figure S2 in the Supporting Information.

The conformation of the organic molecules around the apatite core of the NPs is another key parameter to accurately describe how the corona is organized. Conformation could be deduced by application of Flory's equation, by determining the *Rf*/*D* ratio that depends on the grafting density evaluated above and on the length of the PEG.[41] PEG chains may indeed either "align" in a rather parallel setting—thus exhibiting a comb-like or brush conformation—or, on the contrary, crumble on the surface to form mushroom-like structures. Flory's equation aims at calculating the ratio *Rf*/*D*, where *D* is the average distance between two anchoring points and *Rf* is Flory's radius, which roughly corresponds to the space occupied by the PEG chain on the surface. These two parameters can be determined as follows

$$D = 2(\pi\sigma)^{-\frac{1}{2}} \quad (1)$$

where σ is the surface grafting density (molecules nm^{-2}), determined above by quantitative ERETIC ^{31}P NMR analyses, and

$$Rf = \alpha N^{\frac{3}{5}} \quad (2)$$

where α is the effective monomer length = 0.358 nm for PEG and N is the degree of polymerization, which is deduced from the PEG length. According to the theory behind Flory's equation,[25,41] while an *Rf*/*D* ratio lower than 1 indicates a mushroom conformation, a value greater than 1 is characteristic of a brush regime. Interestingly, for all the NPs obtained, *Rf*/*D* values were significantly greater than 1, thus evidencing a brush

conformation (Table 1) indicating that the organic corona around the NPs allows a good presentation of the ligands on the external surface of the particles which could interact with cell surface receptors, e.g.

To further explore the NPs physicochemical properties, a portion of each colloidal suspension was freeze-dried to perform solid-state characterizations. XRD analyses (Figure S3, Supporting Information) confirmed the apatitic nature of the particles by the presence of characteristic peaks, e.g., (002), (211), (300), and (310), as compared to stoichiometric hydroxyapatite. The broad peaks observed for these hybrid NPs can be linked to the nanometric and probable sub-stoichiometric characters of the apatite phase. Although the P(PEG3K)-NEt_2-decorated NPs (NPs 4) were already weakly crystallized, it seems that the presence of peptides (NPs 7–14) further slowed down apatite crystallization as we obtained an even more weakly crystallized structure (**Figure 3**a reports the illustrative case of the NPs surrounded by P(PEG3K)-RGD (NPs 7) after background correction). It may be noted that modification of the nature of the peptide somewhat influenced the crystallinity of the apatite phase, as illustrated in Figure S3 in the Supporting Information. This may be due to slight differences in the charged end-groups exposed by each peptide, although this did not affect the colloidal stability. Application of Scherrer's equation[42] to lines (002) and (310) for the example of sample NPs 7 (100% P(PEG3K)-RGD stabilizing agent) allowed us to estimate, respectively, the mean crystallite length ≈26 nm and width/depth ≈11 nm, thus confirming again the nanocrystalline character of the apatite phase in presence. Considering the TEM images unveiling the polycrystalline character of each individual NP, it is reasonable to state that the NPs were formed by the strong aggregation of apatite crystallites, the number of which can be controlled through the amount of stabilizing agent use. Apatite crystal agglomeration is indeed a well-known phenomenon, probably due to the high surface energy of "nude" apatite surfaces; and TEM images (e.g., zoom NPs 3, Figure 2a) point out the rather irregular periphery of each individual NP suggesting the existence of smaller primary entities—as schematized in Figure 1—with a size globally of the order of magnitude of the crystallite dimensions.

To estimate the Ca/P molar ratio of the apatite phase composing the NPs, a calcination experiment was also undergone at 1000 °C for 15 h for the NPs 7 stabilized by 100% of P(PEG3K)-RGD. Upon such a thermal treatment, slightly nonstoichiometric apatites should indeed decompose into a mixture of stoichiometric hydroxyapatite (HA, Ca/P = 1.67) and β-tricalcium phosphate (β-TCP, Ca/P = 1.50). Confrontation to a standard curve obtained with known HA/β-TCP mixtures then allowed us to determine the Ca/P molar ratio of the apatite phase present in the NPs, leading to Ca/P ≈ 1.65. This value, slightly lower than the theoretical value of HA, confirmed the nonstoichiometric character of the apatite.

Both the nanocrystalline and nonstoichiometric features found here are key parameters of natural bone apatite. To further examine the apatite phase constituting the mineral core of the NPs, Fourier-transform infrared (FTIR) spectra were recorded. Figure S4 in the Supporting Information shows the typical spectrum of NPs 7 (100% P(PEG3K)-RGD stabilizing agent). Comparison with the NPs 4 stabilized with P(PEG3K)-NEt_2 (i.e., without peptide termination) showed very similar spectral features,

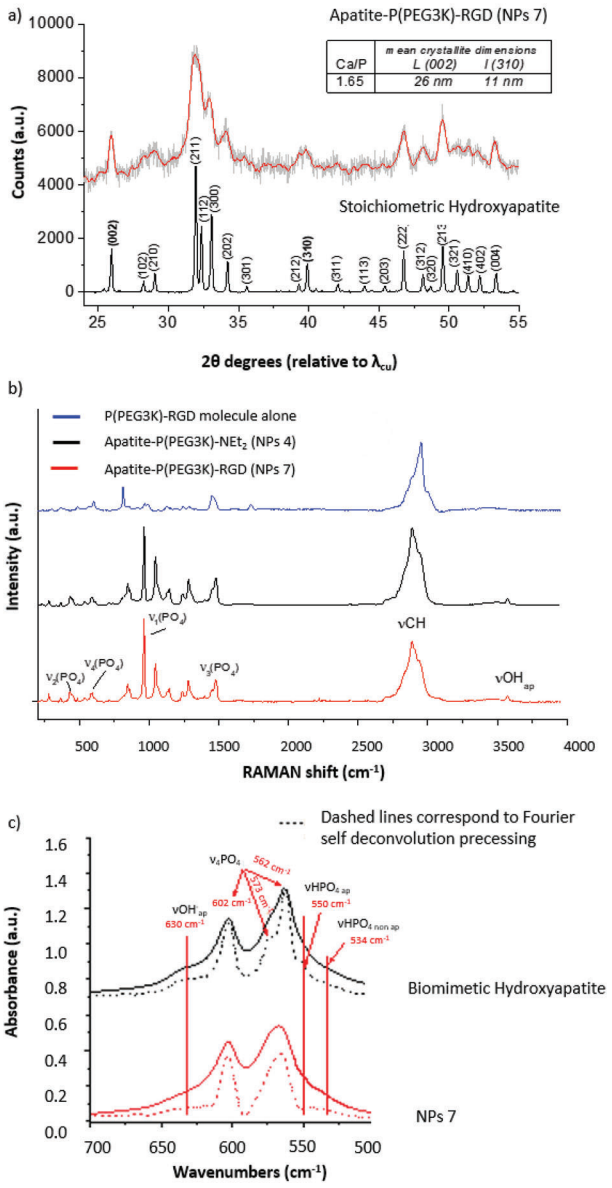

Figure 3. Structural features of colloidal hybrid apatite NPs stabilized by the novel P(PEG3K)-peptide conjugate (case of the RGD peptide) and of related reference compounds: a) XRD pattern, b) Raman shift, and c) FTIR spectrum.

indicating that the peptide moiety did not noticeably affect the apatite phase. This conclusion was also confirmed by Raman microspectroscopy (Figure 3b), pointing to very similar Raman shifts with or without peptide functionalization of the P(PEG) chain. By FTIR, it may additionally be stated that the intensity of the band at 632 cm^{-1} assignable to apatitic OH^- ions appears more pronounced for NPs 7 than for the biomimetic apatite reference, while the HPO_4^{2-} signature appears less visible. These conclusions were confirmed by zooming in the $\nu_4(PO_4)$ domain and upon spectral enhancement treatment via Fourier self-deconvolution (dashed lines in Figure 3c). Therefore, while the apatitic phase appears nonstoichiometric by the presence of

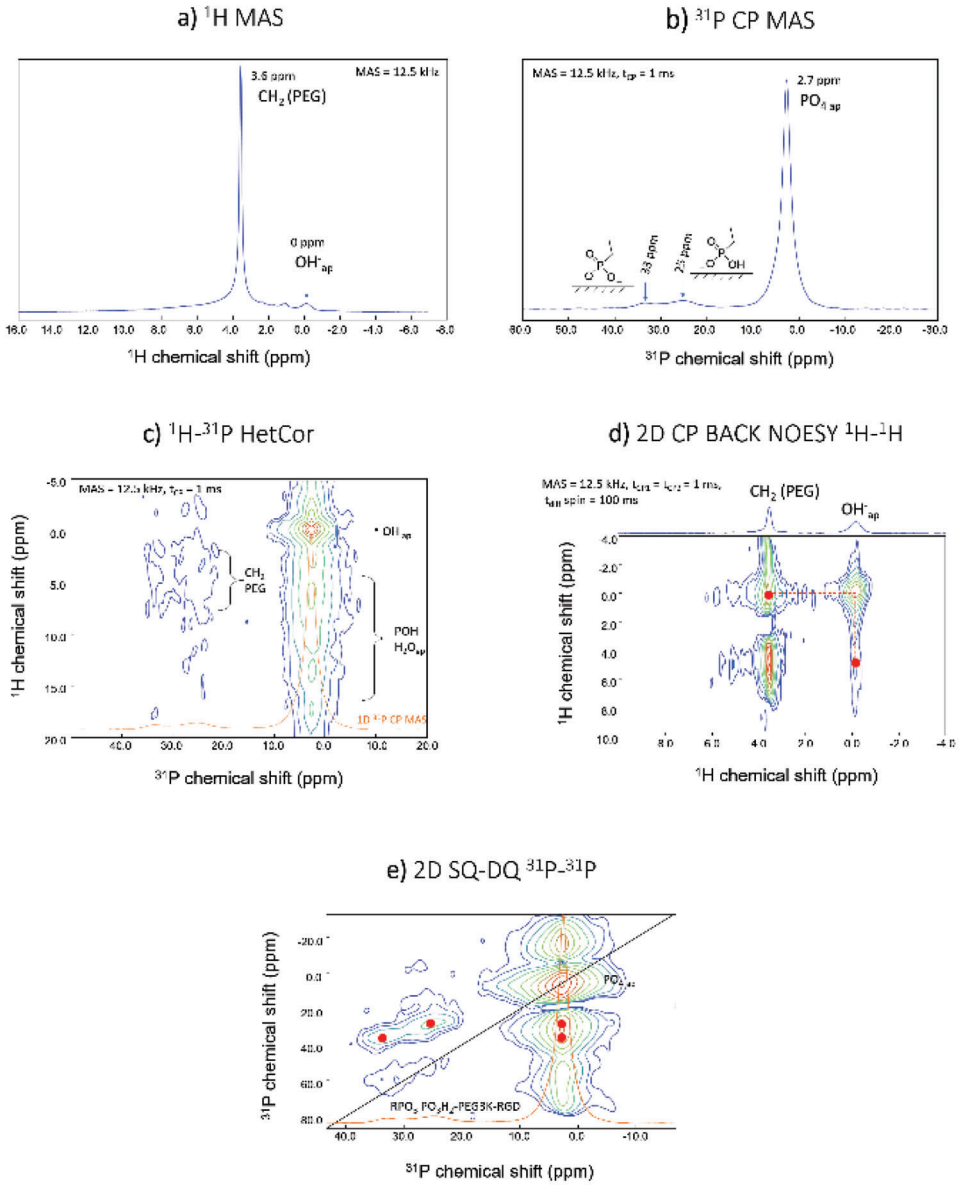

Figure 4. Solid-state NMR analyses of the NPs stabilized by P(PEG3K)-RGD: a) ^{1}H MAS, b) ^{31}P CP MAS, c) ^{1}H-^{31}P HetCor, d) 2D CP BACK NOESY ^{1}H-^{1}H, e) SQ-DQ ^{31}P-^{31}P.

HPO_4^{2-} ions (indicating the protonation of some PO_4^{3-} ions and thus the coexistence of Ca^{2+} vacancies to keep the electroneutrality of the crystals), the HPO_4^{2-} amount remains rather limited. These findings thus indicate that this apatite phase approaches more the characteristics of a rather mature bone mineral,[1] in keeping with its bioinspired character.

Another important question is the mode of anchoring of the organic component onto the apatitic surface. To verify our hypothesis of anchoring through the phosphonate end group of the PEG chain, ^{1}H-^{31}P solid-state NMR (ssNMR) analyses were carried out. By ^{1}H MAS (magic-angle spinning) NMR (direct acquisition), the characteristic resonance of apatitic protons from OH^- ions at $\delta(^{1}H) = 0$ ppm and that of CH_2 groups from P(PEG3K)-RGD at $\delta(^{1}H) = 3.6$ ppm was clearly detected as shown in **Figure 4**a. By ^{31}P cross-polarization (CP) MAS analysis (t_{CP} = 1 ms), the typical signature of apatitic PO_4^{3-} ions was observed at $\delta(^{31}P) = 2.7$ ppm. The CP mode allowed transferring polarization from ^{1}H to ^{31}P in order to increase the sensitivity, which was necessary here as the organic phosphonate groups were only located at the surface sites of apatite particles.

As a result, two additional peaks were noticed at 33 and 25 ppm (Figure 4b) suggesting two modes of surface coordination of the phosphonate group. Since a decrease in chemical shift points to a more condensed phosphate group, the first signal at 33 ppm could correspond to monodentate interaction (≈50% of P(PEG3K)-Peptide according to the integration of the peaks) while the second peak could be related to a more constrained configuration, e.g., bidentate interaction or more

embedded within the apatitic surface lattice. This very strong anchoring of P(PEG3K)-Peptide to the apatite surface was experimentally demonstrated here for the first time and confirmed through ^{31}P NMR liquid quantification experiments which showed that the amount of P(PEG3K)-Peptide anchored around the NPs remained unchanged despite heavy dilution by dialysis.

2D ^{1}H-^{31}P hetero-correlation (HetCor) analysis was then carried out to detect protons close to the P of the apatite phase and close to the organic moiety (Figure 4c). The proton signature from apatitic OH^- at 0 ppm could be visualized as well as some protons characteristic of P-OH groups (typically in HPO_4^{2-} ions from nonstoichiometric apatites) and/or of H_2O, in accordance with the nonstoichiometric character of the apatite phase as evidenced by FTIR. For the organic moiety, the protons from the CH_2 groups linked to P lead to a cross-peak centered around 4–5 ppm. Their large width of this ^{1}H signal could be explained by an increased rigidity of the nearest CH_2 to the surface due to the grafting process. A 2D CP BACK NOESY (nuclear overhauser effect spectroscopy) ^{1}H-^{1}H analysis was subsequently undergone (Figure 4d): in the first dimension (horizontal axis), double CP $^{1}H \rightarrow {}^{31}P \rightarrow {}^{1}H$ allowed polarizing the protons located close to P; in the second dimension, ^{1}H spin diffusion allowed probing the proximity of the protons from the first dimension.[43] In these conditions, the presence of peaks out of the diagonal is indicative of spatial proximity, which is shown here between apatitic OH^- and some CH_2 groups from PEG. This result agrees well with the grafting of the P(PEG3K)-RGD molecule at the surface of apatite. Finally, a 2D SQ-DQ ^{31}P-^{31}P analysis was run (SQ and DQ standing, respectively, for single quantum and double quantum) to probe only very short distances between ^{31}P (< 5–6 Å) by re-introducing the ^{31}P-^{31}P dipolar interaction (Figure 4e). Peaks positioned out of the diagonal are then informative on ^{31}P-^{31}P proximity. Here, we could identify clear correlation domains between P from P(PEG3K)-RGD and P from apatite, thus confirming the success of the anchoring procedure via the phosphonate end group. This was valid for both modes of anchoring, namely, mono- (only graft at the apatite surface) and bidentate/constrained (is a part of apatite lattice).

Taken together, these characterizations showed that the core of hybrid particle is composed of bone-inspired nanocrystalline apatite; whereas the organic corona bears a phosphonate end-group that efficiently interacts with the apatitic surface to provide colloidal stabilization with controlled particle size/shape. The peptide moiety is exposed at the other end of the conjugate forming a corona accessible for biological interactions.

The biocompatibility and the bioactivity of the hybrid P(PEG3K)-RGD or P(PEG3K)-YIGSR apatite NPs (respectively, NPs 7 and 11) were assessed in vitro using NIH/3T3 mouse fibroblasts. To observe the influence of each part of the hybrid NPs such as peptides, P(PEG3K)-Peptide and NPs stabilized with P(PEG3K)-NEt_2 (NPs 4) were tested. Wells were also devoted to control without any NPs. For these experiments, the highest peptide concentration studied corresponded to the initial concentration found in NPs 7 and 11 suspensions from the above liquid-state NMR analyses (2.25×10^{-3} and 1.91×10^{-3} M, respectively). These concentrations were in agreement with the literature which reports the efficiency of RGD-peptide and YIGSR-peptide sequences for fibroblasts migration and proliferation with a concentration ranging from 1×10^{-3} to 3×10^{-3} M.[28,29] The results were read after 72 h of incubation and six replicates were performed.

As seen from the relative metabolic activity of the treatment groups versus controls reported in **Figure 5**a, the NPs 7 and 11 with, respectively, an P(PEG3K)-RGD or P(PEG3K)-YIGSR corona were found to be fully biocompatible (cell viability > 70% according to the ISO 10993–5 standard) and had no negative effect on cell viability, assessed by the metabolic assay. This may probably be related to the high bioinspired character of these NPs arising from both their inorganic (bone-like apatite) and organic (peptides) components. Also, interestingly, the two types of NPs (NPs 7 and 11) appeared to induce a proliferative effect over the 72 h tested, as evidenced by a net increase in cell number relative to the control performed without NPs or corona components. Additionally, a synergistic effect of each part of the multicomponent NPs—, i.e., the apatite phase on the one hand and the peptide on the other hand—was observed (Figure 5a), and together they considerably increased the proliferation of the cells.

The proliferation effect of the NPs was further examined in a second assay that measured the metabolic activity of NIH/3T3 cells over time on days 1, 3, and 5, using mid-range peptide doses tested in the biocompatibility assays, namely, 1.13×10^{-3} M for RGD and 0.96×10^{-3} M for YIGSR. The NPs were adherent to the cells with visible accumulation by the 24 h time point (Figure 5b). These enhanced proliferative properties can clearly be attributed to the presence of the peptide terminations on the stabilizing agents around the NPs, as the P(PEG3K)-NEt_2 stabilizer itself did not show this proliferation (NPs 4) tendency as indicated by the rather stable number of fibroblast cells in this case. These results remind other results from the literature (on different types of biomaterials) pointing out the potentially pro-proliferative character of such peptide sequences[44,45] for fibroblast cells.

These findings agree well with our physicochemical analyses showing that the P(PEG3K)-Peptide molecules were grafted in brush regime to the apatite particles through their phosphonate end-group and exposed on the other end the peptide moieties toward the surrounding medium. These results thus evidence that the peptide functionalization process developed in this work did not inhibit peptide activity, and instead provided a way to expose them efficiently to cells present in the medium.

3. Concluding remarks

In this work, colloidal stabilization of biomimetic apatite nanoparticles and biofunctionalization was achieved through one-pot co-precipitation strategy using phosphonated PEG peptide conjugates. We demonstrated that i) the hybrid apatite-peptide nanoparticles had a monomodal size distribution controlled by the organic moiety used as stabilizing agent, ii) the inorganic core of the NPs was composed of bioinspired calcium phosphate apatite, iii) the anchoring of the organic stabilizing conjugates proceeded through the phosphonate end group as mono- and bidentate/constrained surface complexes, iv) the conjugates were exposed in a brush conformation allowing for efficient exposition of the peptides to the outer periphery of the NPs, and v) the NPs were biocompatible and exerted pro-proliferative biological effect on fibroblasts thanks to their functionalization with relevant bioactive peptides.

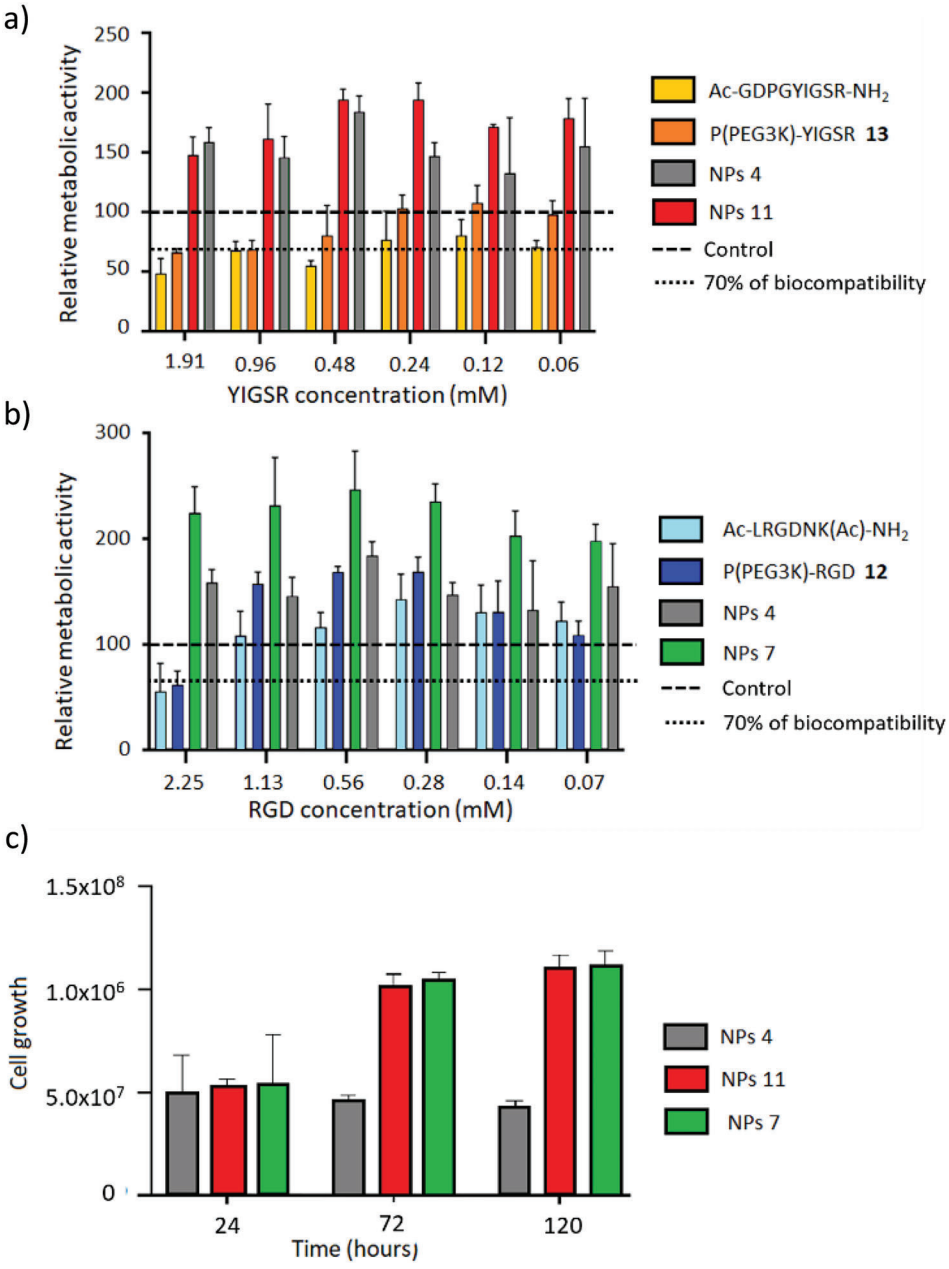

Figure 5. NIH/3T3 fibroblast cell viability/metabolic activity for NPs stabilized with a) P(PEG3K)-RGD (NPs 7) and b) P(PEG3K)-YIGSR (NPs 11) after 72 h and c) proliferation experiments at 0.1 mM of peptide.

Beyond this proof of concept, this synthetic strategy allows to access to a family of structurally and functionally well-defined hybrid peptide apatite NPs as tailorable, multifunctional bioactive nanosystems. From an applicative biomedical viewpoint,[46] peptide-functionalized compounds can offer tunable properties in nanomedicine, whether for diagnostics (using fluorescent peptides) and therapeutic (e.g., antibacterial peptides) applications,[47] for use in bio-sensing and regenerative medicine. Peptide-decorated apatite NPs could, e.g., be envisioned in the field of dermatology (e.g., for wound healing) or for bone repair, in combination with a support matrix.

Supporting Information

Supporting Information is available from the Wiley Online Library or from the author.

Acknowledgements

C.D. and G.S. contributed equally to this work. This research, including the Ph.D. grant of Mathilde Guérin, was funded by the Institute Carnot Chimie Balard Cirimat through the ANR program no. 16 CARN 0008-01. The authors acknowledge the technical and human support provided by

the analytical facilities, "Laboratoire de Mesures Physiques" of the University of Montpellier and of the IBiSa SynBio3 Platform.

Conflict of Interest

The authors declare no conflict of interest.

Data Availability Statement

The data that support the findings of this study are available in the Supporting Information of this article.

Keywords

biomimetic phosphocalcic apatite, hybrid peptide-apatite materials, nanoparticles, peptides, one-pot synthesis

Received: July 26, 2023
Published online:

[1] J. Gómez-Morales, M. Iafisco, J. M. Delgado-López, S. Sarda, C. Drouet, *Prog. Cryst. Growth Charact. Mater.* **2013**, *59*, 1.
[2] B. Wang, Z. Zhang, H. Pan, *Biomimetics* **2023**, *8*, 90.
[3] J. S. Earl, D. J. Wood, S. J. Milne, *J. Phys.: Conf. Ser.* **2006**, *26*, 268.
[4] Z. Bal, T. Kaito, F. Korkusuz, H. Yoshikawa, *Emergent Mater.* **2020**, *3*, 521.
[5] S. Bose, S. Tarafder, A. Bandyopadhyay, in *Hydroxyapatite (Hap) Biomedical Applications*, (Ed.: M. Mucalo), Elsevier, New York, **2015**, pp. 143–157.
[6] D. Arcos, M. Vallet-Regí, *J. Mater. Chem. B* **2020**, *8*, 1781.
[7] C. G. Weber, M. Mueller, N. Vandecandelaere, I. Trick, A. Burger-Kentischer, T. Maucher, C. Drouet, *J. Mater. Sci.: Mater. Med.* **2014**, *25*, 595.
[8] H. Autefage, F. Briand-Mesange, S. Cazalbou, C. Drouet, D. Fourmy, S. Goncalves, J. Salles, C. Combes, P. Swider, C. Rey, *J. Biomed. Mater. Res., Part B* **2009**, *529-530*, 475.
[9] M. Iafisco, F. Carella, L. Degli Esposti, A. Adamiano, D. Catalucci, J. Modica, A. Bragonzi, A. Vitali, R. Torelli, M. Sanguinetti, F. Bugli, *J. Inorg. Biochem.* **2022**, *230*, 111751.
[10] S. Hossain, H. Yamamoto, E. H. Chowdhury, X. Wu, H. Hirose, A. Haque, Y. Doki, M. Mori, T. Akaike, *PLoS One* **2013**, *8*, e60428.
[11] M.-A. Pizzoccaro, O. Nikel, S. Sene, C. Philippe, P. H. Mutin, S. Bégu, D. Vashishth, D. Laurencin, *Acta Biomater.* **2016**, *41*, 342.
[12] C. A. S. D. Souza, A. P. V. Colombo, R. M. Souto, C. M. Silva-Boghossian, J. M. Granjeiro, G. G. Alves, A. M. Rossi, M. H. M. Rocha-Leão, *Colloids Surf., B* **2011**, *87*, 310.
[13] S. Sarda, F. Errassifi, O. Marsan, A. Geffre, C. Trumel, C. Drouet, *Mater. Sci. Eng., C* **2016**, *66*, 1.
[14] R. A. Nadar, N. Margiotta, M. Iafisco, J. J. J. P. Van Den Beucken, O. C. Boerman, S. C. G. Leeuwenburgh, *Adv. Healthcare Mater.* **2017**, *6*, 1601119.
[15] S. Cazalbou, G. Bertrand, C. Drouet, *J. Phys. Chem. B* **2015**, *119*, 3014.
[16] M. Iafisco, J. M. Delgado-Lopez, E. M. Varoni, A. Tampieri, L. Rimondini, J. Gomez-Morales, M. Prat, *Small* **2013**, *9*, 3834.
[17] M. Iafisco, E. Varoni, M. Di Foggia, S. Pietronave, M. Fini, N. Roveri, L. Rimondini, M. Prat, *Colloids Surf., B* **2012**, *90*, 1.
[18] C. Drouet, *Intern. Med. Primary Healthcare* **2015**, *1*, 1.
[19] A. Bouladjine, A. Al-Kattan, P. Dufour, C. Drouet, *Langmuir* **2009**, *25*, 12256.
[20] M. Choimet, A. Tourrette, O. Marsan, G. Rassu, C. Drouet, *Acta Biomater.* **2020**, *111*, 418.
[21] M. Stefanic, K. Ward, H. Tawfik, R. Seemann, V. Baulin, Y. Guo, J.-B. Fleury, C. Drouet, *Biomaterials* **2017**, *140*, 138.
[22] S. Sarda, M. Iafisco, P. Pascaud-Mathieu, A. Adamiano, M. Montesi, S. Panseri, O. Marsan, C. Thouron, A. Dupret-Bories, A. Tampieri, C. Drouet, *Langmuir* **2018**, *34*, 12036.
[23] M. J. Chua, S. Tiash, T. Fatemian, M. I. Noordin, C. S. Keng, E. H. Chowdhury, *OA Cancer* **2013**, *1*, 7.
[24] M. Miragoli, P. Ceriotti, M. Iafisco, M. Vacchiano, N. Salvarani, A. Alogna, P. Carullo, G. B. Ramirez-Rodríguez, T. Patrício, L. D. Esposti, F. Rossi, F. Ravanetti, S. Pinelli, R. Alinovi, M. Erreni, S. Rossi, G. Condorelli, H. Post, A. Tampieri, D. Catalucci, *Sci. Transl. Med.* **2018**, *10*, eaan6205.
[25] M. Maurel, T. Montheil, J. Martin, L. Chaar, V. Guzman-Gonzalez, M. Couvet, T. Jacquet, T. Jia, B. Eymin, K. Parra, P. Dumy, J. Martinez, F. Ruggiero, E. Vaganay, A. Mehdi, J.-L. Coll, G. Subra, *Nanomaterials* **2021**, *11*, 177.
[26] J. S. Suk, Q. Xu, N. Kim, J. Hanes, L. M. Ensign, *Adv. Drug Delivery Rev.* **2016**, *99*, 28.
[27] M. D. Pierschbacher, E. Ruoslahti, *Nature* **1984**, *309*, 30.
[28] S. Y. Boateng, S. S. Lateef, W. Mosley, T. J. Hartman, L. Hanley, B. Russell, *Am. J. Physiol.: Cell Physiol.* **2005**, *288*, C30.
[29] L. Battistini, K. Bugatti, A. Sartori, C. Curti, F. Zanardi, *Eur. J. Org. Chem.* **2021**, *2021*, 2506.
[30] T. G. Kapp, F. Rechenmacher, S. Neubauer, O. V. Maltsev, E. A. Cavalcanti-Adam, R. Zarka, U. Reuning, J. Notni, H.-J. Wester, C. Mas-Moruno, J. Spatz, B. Geiger, H. Kessler, *Sci. Rep.* **2017**, *7*, 39805.
[31] D. S. Grant, K. Tashiro, B. Segui-Real, Y. Yamada, G. R. Martin, K. Kleinman, *Cell.* **1989**, *58*, 933.
[32] S. P. Massia, J. A. Hubbell, *J. Cell Biol.* **1991**, *114*, 1089.
[33] G. Laconde, M. Amblard, J. Martinez, *Tetrahedron Lett.* **2019**, *60*, 341.
[34] D. Mustafa, J. M. Overhulse, B. A. Kashemirov, C. E. Mckenna, *Molecules* **2023**, *28*, 3497.
[35] A. J. Gutierrez, E. J. Prisbe, J. C. Rohloff, *Nucleosides, Nucleotides Nucleic Acids* **2001**, *20*, 1299.
[36] S. R. Houghton, J. Melton, J. Fortunak, D. H. Brown Ripin, C. N. Boddy, *Tetrahedron* **2010**, *66*, 8137.
[37] K. Justyna, J. Malolepsza, D. Kusy, W. Maniukiewicz, K. M. Blazewska, *Beilstein J. Org. Chem.* **2020**, *16*, 1436.
[38] K. M. Blazewska, *J. Org. Chem.* **2014**, *79*, 408.
[39] A. Al-Kattan, P. Dufour, J. Dexpert-Ghys, C. Drouet, *J. Phys. Chem. C* **2010**, *114*, 2918.
[40] A. Al-Kattan, P. Dufour, C. Drouet, *Colloids Surf., B* **2011**, *82*, 378.
[41] L. Adumeau, C. Genevois, L. Roudier, C. Schatz, F. Couillaud, S. Mornet, *Biochim. Biophys. Acta, Gen. Subj.* **2017**, *1861*, 1587.
[42] P. Scherrer, *Nachr. Ges. Wiss. Goettingen, Math.-Phys. Kl.* **1918**, *1918*, 98.
[43] S. Von Euw, W. Ajili, T.-H.-C. Chan-Chang, A. Delices, G. Laurent, F. Babonneau, N. Nassif, T. Azaïs, *Acta Biomater.* **2017**, *59*, 351.
[44] X. Z. Shu, K. Ghosh, Y. Liu, F. S. Palumbo, Y.i Luo, R. A. Clark, G. D. Prestwich, *J. Biomed. Mater. Res., Part A* **2004**, *68A*, 365.
[45] Y. Kumada, N. A. Hammond, S. Zhang, *Soft Matter* **2010**, *6*, 5073.
[46] A. Khalili, M. Ahmad, *Int. J. Mol. Sci.* **2015**, *16*, 18149.
[47] N. Alvisi, R. De Vries, *Mater. Today Bio* **2023**, *19*, 100580.

